Hindawi
Journal of Nanomaterials
Volume 2023, Article ID 7267093, 11 pages
https://doi.org/10.1155/2023/7267093

Research Article

Investigation of Mechanical Behavior and Surface Characteristics of Cold Spray Metallized B_4C/AA7075 Composites Coated by AZ64 Alloy through Plasma Electrolytic Oxidation

Selvakumaran Thunaipragasam,[1] Aniket Bhanudas Kolekar,[2] Koli Gajanan Chandrashekhar,[3] Rohit Pandey,[4] Mohammad Shahid,[5] K. Rajesh,[6] P. Ragupathi,[7] Asheesh Kumar,[8] and Balkeshwar Singh[9]

[1]*Department of Aerospace Engineering, SRM Institute of Science and Technology, Kattankulathur 603203, Chennai, India*
[2]*Department of Mechanical Engineering, Dr. D Y Patil Institute of Engineering Management and Research, Pune 411044, India*
[3]*Department of Mechanical Engineering, Sanjeevan Engineering and Technology Institute, Kolhapur 416201, India*
[4]*Department of Mechanical Engineering, Amity University Madhya Pradesh, Maharajpura Dang, Gwalior 474005, Madhya Pradesh, India*
[5]*Department of Electrical Engineering, Galgotias College of Engineering and Technology, Greater Noida, Uttar Pradesh, India*
[6]*Department of Physics, Academy of Maritime Education and Training (Deemed to be University), 135, East Coast Road, Kanathur 603112, India*
[7]*Department of Mechanical Engineering, Karpagam Academy of Higher Education (Deemed to be University), Pollachi Main Road, Eachanari, Coimbatore 641021, India*
[8]*Department of Mechanical Engineering, Mahatma Gandhi Institute of Technology, Hyderabad, India*
[9]*Department of Mechanical Design and Manufacturing Engineering, Adama Science and Technology University, Kebele-14, Adama 1888, Ethiopia*

Correspondence should be addressed to Balkeshwar Singh; balkeshwar.singh@astu.edu.et

Received 17 August 2022; Accepted 20 September 2022; Published 20 April 2023

Academic Editor: Ramesh Balasubramanian

Metallized cold-spray coatings were employed to make B_4C/AA7075 and aluminum + plasma electrolytic oxidation (PEO) duplex coatings on AZ64. In addition, the phase structure, mechanical characteristics, wear, and PEO ceramic coatings examine the corrosion resistance. According to the findings, the PEO ceramic coating comprises α-aluminum oxide and γ-aluminum oxide, with some remnants of B_4C still being preserved. PEO ceramic coatings outperformed their corresponding CS counterparts regarding mechanical characteristics and wear resistance. For example, the PEO-B_4C coating achieved a hardness of 13.8 GPa and an elastic modulus of 185.5 GPa, which were 21.0% and 23.5%, respectively, more significant than the comparable values for the coating with CS. The PEO-B_4C coating was 58% and 15.7% less abrasive than the equivalent CS coating due to its lower wear rate of 4.84×10^{-5} mm^3/Nm and relatively lower of 0.64. The density of corrosion current in the PEO-treated B_4C-AA7075 coating (3.735×10^6 A/cm^2) is similar to the corrosion current density in the untreated CS coatings. Finally, compared to untreated CS B_4C-AA7075, the coating's mechanical characteristics and wear resistance are considerably enhanced by the PEO treatment.

1. Introduction

Roughening components and low surface energy are combined to form an SH surface with a water contact angle (WCA) of more than 150° when PVC binder in THF solvent is mixed with roughening components (referred to as "superhydrophobic") [1]. Since AZ91 alloys are not very hard, corrosion resistant, and wear resistant, they are used in high-stress technical applications [2, 3]. Material characteristics improve by employing a wide variety of surface engineering techniques. It is called CS, and it is a new way to alter textures [4–6]. While still in solid, CS particles

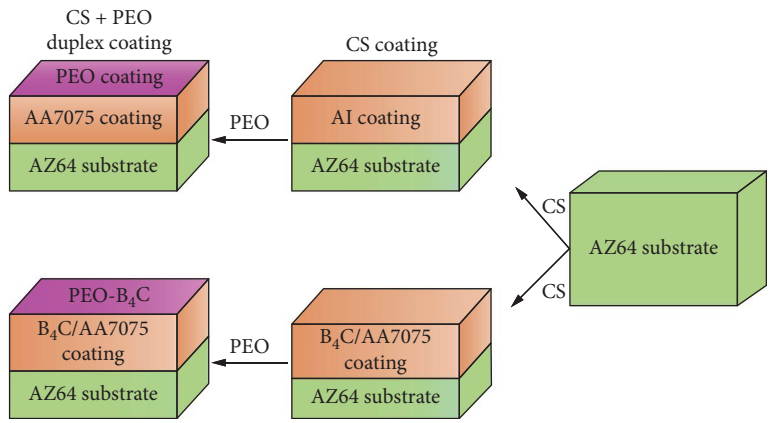

Figure 1: Al + PEO and B_4C-AA7075 + PEO duplex coating preparation schemes.

deposit on the substrate with significant kinetic energy. This technique is better than conventional thermal spray methods due to its comparatively "cool" working gas temperature [7]. Therefore, high-temperature exposures such as those seen in ovens and microwaves can be avoided, along with the resulting oxidation, melting, phase changes, etc. [8]. Many alloys analyze with CS deposits for surface protection, including Al, Al_2O_3-Al, ND-Al, and B_4C-AA7075 [9]. The CS coating's resistance to wear and corrosion is not up to par with the rigorous requirements of the many applications and environmental circumstances [10].

The plasma electrolytic oxidation (PEO) deposition method results in a ceramic sheathing that dramatically increases the wear and hardness of softer and more malleable metals, including aluminum, magnesium, Ti, and their alloys [11]. The Al_2O_3 oxide converting layer produced by the PEO method significantly enhances the resistance to wear and corrosion of aluminum and related alloys, as demonstrated by many studies [12–14]. As a result of these findings, a hybrid CS + PEO dual coating technique is to develop a hard metallurgically supporting ceramics surface. PEO technology turns the metallic coating into a ceramic coating after it applies to the substrate with CS [15]. Using a CS and PEO method, coated AZ31 alloy with an aluminum-based PEO layer [16]. The aluminum-based PEO coating improved wear resistance by 87% compared to an Al coating and had corrosion resistance on par with pure aluminum [17–19]. Analyses were performed on the two CS + PEO dual coatings to determine their microstructure, mechanical characteristics, phase composition, wear, corrosion, and abrasion resistance [20, 21]. Duplex coating, generally protected by magnesium and its coatings, particularly Al_2O_3, showed superior resistance to wear and corrosion (an improvement of 61% on the order of magnitude for each property). A duplex coating provides hybrid, unique, and efficient surface protection for alloys used in demanding situations by fusing the CS and PEO processes [22]. However, there is a lack of literature on this hybrid process. The CS B_4C-AA7075 and aluminum coatings applied on AZ64 were employed as seed surfaces and subjected to PEO treatment to create the corresponding duplex coatings [23–25]. Microstructure, mechanical characteristics, and phase composition of two CS + PEO duplex coatings were analyzed, as their resistance to wear, corrosion, and abrasion [26, 27]. The two duplex coatings outperform conventional CS coatings in protecting AZ64 alloy substrates. It must be noted that the first and only paper to describe the use of PEO treatment to produce an additional layer of protection on top of an existing CSP coating (CS B_4C-AA7075).

In this research, metallized cold-spray coatings were used to produce the composite structures of boron carbide with AA7075 and PEO with aluminum coatings on the AZ64 magnesium alloy. The mechanical behavior, phase structure, and wear and PEO ceramic coatings were used to examine the corrosive resistance.

2. Experimental Procedure

Pure Al powder (D50 = 34 μm) and B_4C-AA7075 composite (D50 = 37 μm) as CS's powder raw materials. As a percentage of the total mass, B_4C made up 1% of the composite powder, and its average particle size ranged from 10 to 50 nm. The SST-P CGDS system applies coatings of CS. The spray angle, pressure, and temperature were set to 90° at 1.7 MPa and 350°C, using nitrogen as the gas phase. Methods for preparing CS coatings (such as Al coating and B_4C-AA7075 coating) are explained in greater depth elsewhere. PEO coating refers to a coating made from PEO-treated Al, and PEO-B_4C coating refers to a coating made from PEO and B_4C on AA7075 (the substrate/seed material). A 15 kW pulse power source was used to run the PEO machinery. For 10 min, the samples were subjected to a PEO treatment with a continuous 0.6 A/0.3 A positive/negative current [28].

The wavelength of the yield was 2,000 Hz, and the duty ratio was 8 g of $NaAlO_2$ per liter of potassium hydroxide, 2 g of sodium ethylenediaminetetraacetic acid per liter, and 2 g of sodium ($Na_3C_6H_5O_{7.2}$) in water in the electrolyte. Figure 1 shows how Al + PEO and B_4C-AA7075 + PEO duplex coatings are created. Using a Miniflex 600 XRD with copper-Kα radiation ($\lambda = 1.5420$) at 41 kV and 16 mA, it also determined the phase compositions of the materials.

The coating's hardness and elasticity evaluate by a battery of nanomechanical properties (UNHT + MCT + MST). A Berkovich diamond indenter applies a force that gradually increases to 10 mN in 30 s during the nanoindentation test. Then, the burden slowly carried down to zero. The corrosion

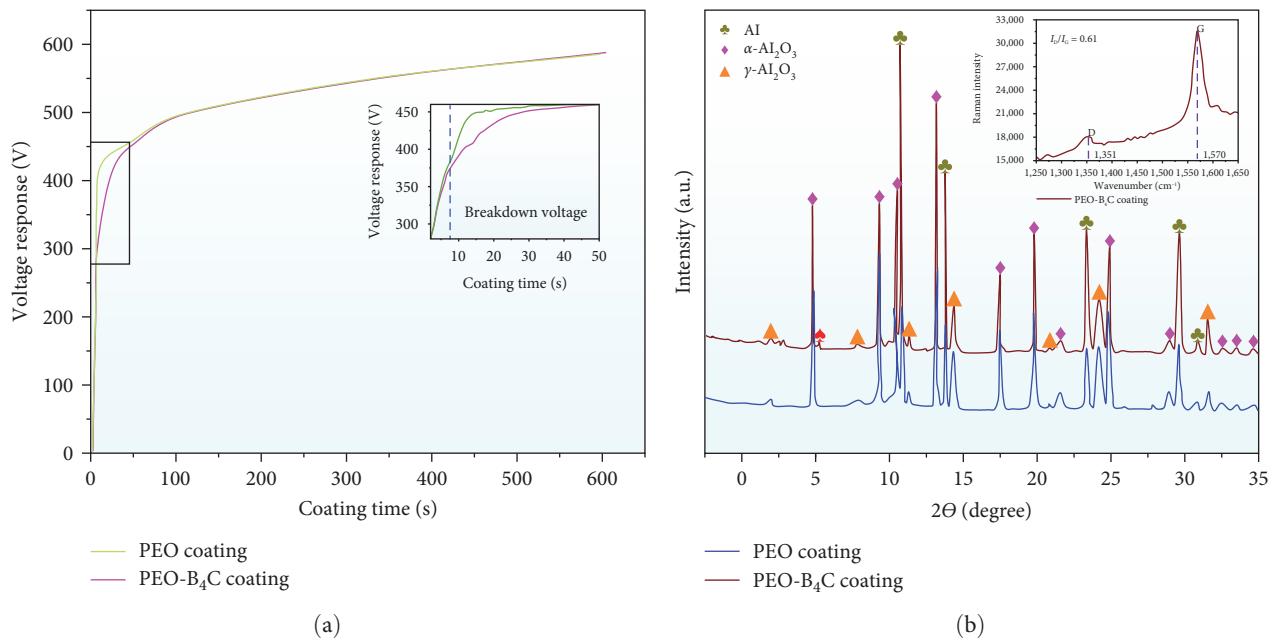

Figure 2: (a) Time–voltage response and (b) XRD pattern.

process testing (ASTM G59-97) was performed at room temperature in a 3.6 wt% NaCl utilizing the CHI600C electrochemical workstation. The sample is the working electrode in a constant potential setup that includes a platinum reference plate and an additional platinum plate. After 30 min in the solution, the open circuit voltage potential was steady enough to conclude the sample. During the polarization scan, the input potential was scanned from −600 to +1,600 mV OCP at a rate of 1 mV/s. Two duplexes' coatings focus on the slide-wearing test (ASTM G99-17) utilizing a test for wear and friction using a ball-disk HT-1000 device at room temperature [29]. The counterbody was a 6 mm Al_2O_3 ball. Test conditions included a load of 2 N applied in a circular motion along a 3 mm radius wear track. It slided the coatings at 300 rpm for 20 min. It determined the volumetric wear rate after measuring the cross-sectional zone with a 3D digital microscope and describing the wear track's morphology.

3. Results

3.1. Phase Composition of the Microstructure. PEO ceramic coating development using the time–voltage response curve is shown in Figure 2(a). Early on in PEO treatment, the effect of the Al_2O_3 coating was demonstrated by a sudden rise in the voltage response [30]. Microdischarge happened when the voltage response was close to the drain current (seen in the inset of Figure 2(a)), slowing the voltage reaction increase and leading to stable saturation voltage. With its high thermal and electrical conductivity, B_4C reduces the breakdown voltage in a B_4C-AA7075 matrix from ∼301 to ∼262 V. As a result, the B_4C-AA7075 coating reached the breakdown voltage much faster during the PEO process than the pure Al coating. Figure 2(b) shows the PEO and PEO-B_4C coatings' on X-ray diffraction (XRD) patterns. Both α-aluminum oxide and γ-aluminum oxide form aluminum oxide in all PEO ceramic coatings. There were also traces of Al and B_4C peaks in the diffraction patterns. It is possible that the carbon peak created from the B_4C-AA7075 coating beneath the PEO-B_4C one, considering how deeply the X-rays penetrate the PEO-B_4C coating. Raman spectroscopy confirmed the presence of graphitic C ($I_D/I_G = 0.61$) in the PEO-B_4C layer (shown as an inset in Figure 2(b)).

It indicates that the PEO procedure has a negligible effect on the B_4Cs stability. The B_4C from the PEO-B_4C coating was, thus, successfully retained in the B_4C-AA7075 coating. Figures 3(a) and 3(d) show the micrographs of cross sections of aluminum + PEO and B_4C-AA7075 + PEO duplex coatings. PEO ceramic coatings make solid, gap-free contact with their substrates. Figures 3(a) and 3(d) show the measured thickness of 315 and 313 m for the Al + PEO and B_4C-AA7075 + PEO duplex coatings. On average, PEO-B_4C coatings were 25 m thicker than PEO coatings (18vs. 5 μm).

The PEO-B_4C coating took longer to mature because of its smaller drain current than AA7075 (Figure 2(a)). Therefore, PEO-B_4C coating was significantly more robust than PEO coating. Cross-sectional analysis reveals that the PEO-B_4C coating consists of two distinct layers [31]. The surface was pocked with pores and fractures, while the interior was considerably thicker. Figure 3(b)–3(e) depicts the surface morphology of PEO and PEO-B_4C coatings. The PEO ceramic coatings had the same rough texture, fractures, and pancake-like porosity lamellar structure. The lamellar pores provided vents for the molten Al_2O_3. An apparent volcanic structure formed around the pores as the Al_2O_3 solidified [32]. The PEO-B_4C coating has higher and finer volcanic peaks than the PEO coating. During PEO, B_4C raised the pressure and temperature locally within the discharge channel [33].

As molten Al_2O_3 poured out of the composite coating's discharge channel, more coating vanished. The EDS scan

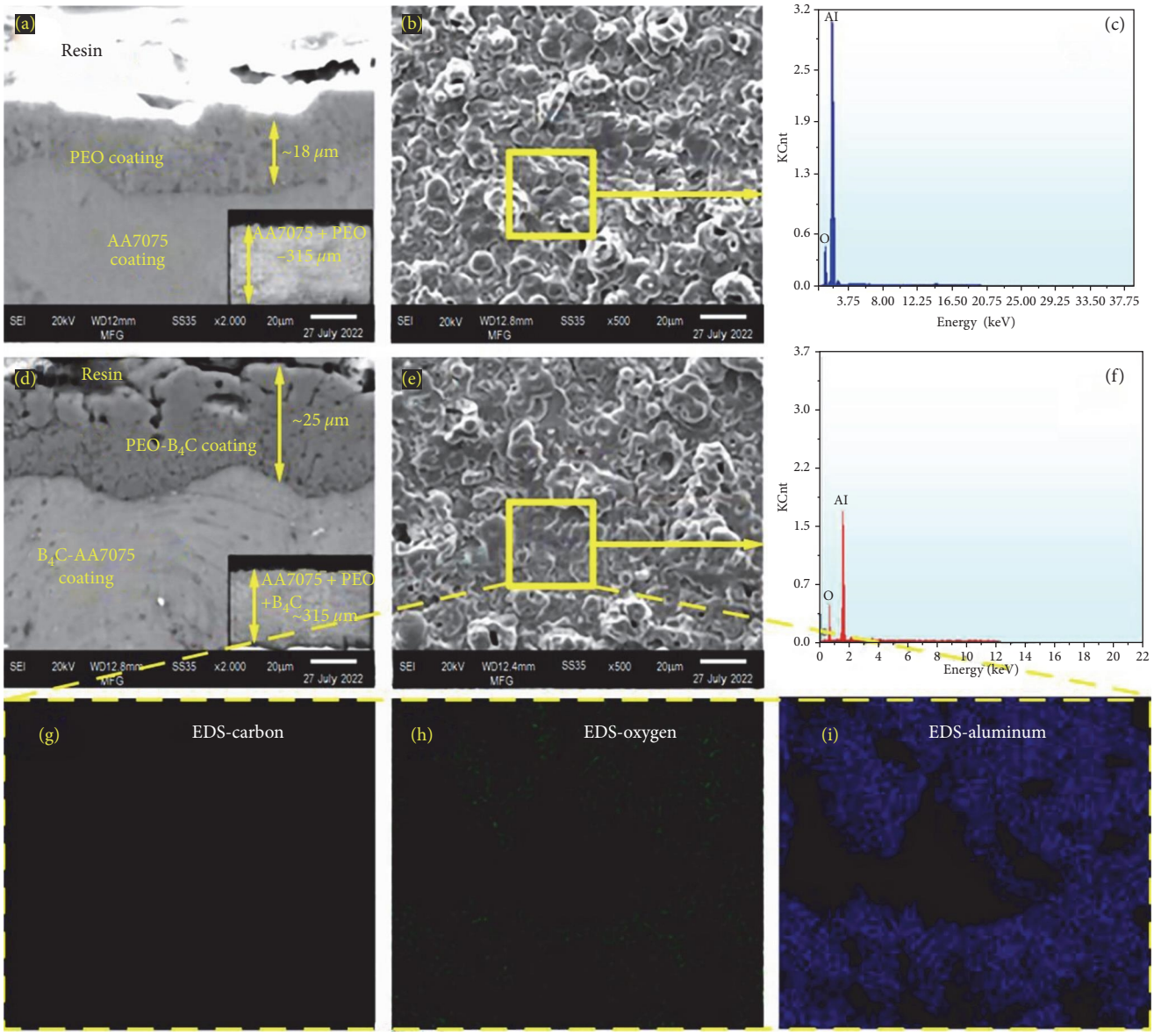

FIGURE 3: SEM images (a, d) cross section, (b, e) surface characteristics, and EDS of (c) PEO coating, (f) PEO-B_4C duplex coating, (g) EDS-carbon, (h) EDS-oxygen, and (i) EDS-aluminum dispersal, as shown in Figure 3(e).

revealed carbon uniformly dispersed throughout the PEO-B_4C coating (Figures 3(c) and 3(f)). C, O, and Al EDS plots are shown in Figure 3 (an expanded portion of Figure 3(e)–3(i)). The EDS scan has revealed carbon dispersed uniformly throughout. It emphasized that the PEO ceramic coating, not CS coating, is the source of the O in the sample. Carbon has a relatively similar distribution pattern to that of O and Al. The element-free zone in EDS maps results from spatial inhomogeneity in the sampling area. It noted that the PEO ceramic coating, not the CS layer, is the source of O in the sample.

3.2. Test Results on Surface Roughness. Figure 4 depicts the R_a value of PEO coating materials. It discovered that PEO-B_4C coating had a rougher surface than PEO coating. The PEO process causes the B_4C-AA7075 coating to produce more molten Al_2O_3, which helps to form crater-like forms on the coating's surface. Consequently, PEO-B_4C coating had a rougher texture than PEO coating. The scanning electron microscopy (SEM) pictures and roughness test results support this (Figures 3(b) and 3(e)).

3.3. Mechanical Characteristics. To evaluate the nanomechanical characteristics of cold-sprayed metallized and PEO ceramic coatings, researchers ran identical tests on all samples, removing factors such as loading and unloading rate and load. The B4C-AA7075 composite material's mechanical characteristics are evaluated using low nanoindentation stress. PEO ceramic coating thickness was also down, making it unsuitable for heavy weights. Accordingly, the nanoindentation tests were

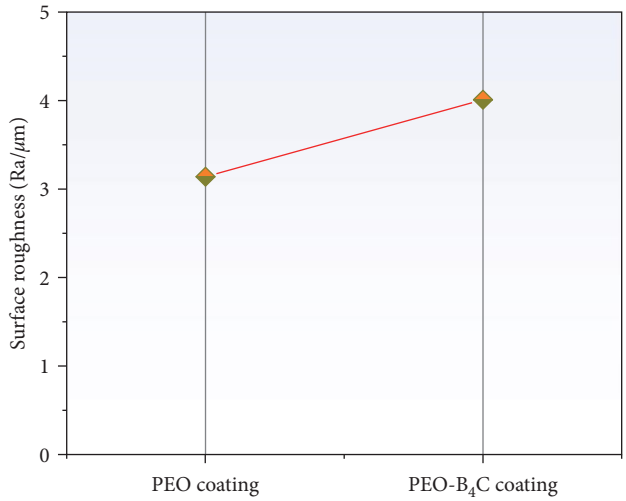

Figure 4: Surface roughness.

conducted with a notional load of 10 mN on AA7075 substrates coated with CS or PEO ceramics, displacement–load curve, nanohardness, and flexion modulus, as shown in Figure 5.

The PEO-B_4C coating improved the material's properties by 23.5% in hardness (13.8 GPa) and 21.6% in elastic modulus (185.4 GPa) compared to the PEO coating. As expected, PEO treatment significantly enhanced the CS coating's mechanical characteristics. Furthermore, the mechanical properties were significantly affected by the PEO-treated B_4C-AA7075 coating as opposed to the PEO-treated AA7075 coating.

3.4. Wear Resistance. Figure 6(a) shows the dry sliding wear rates and coefficient of frictions (COFs) for a PEO ceramics coating on an AZ64 alloy substrate with a CS coating. Figure 6(a) shows that PEO ceramic coatings have slightly lower COF than their CS counterparts. The COF of PEO ceramic coatings increased in the early stages. After a brief rise in the second phase, the COF remained relatively stable. Compared to PEO, the COF of the PEO-B_4C coating is lesser (0.66 and 0.78). In addition, its COF shows lower steady-state variability. The PEO ceramic coating considerably reduced the wear rate compared to a similar CS layer. The PEO-B_4C coating significantly reduced the wear rate to 4.84×10^5 mm^3/Nm compared to the PEO coating. PEO treatment substantially enhances the CS coating's resistance to wear.

3.5. Corrosion Resistance. The optical constant of refraction (OCR) and PDP curves of PEO, as well as PEO-B_4C coatings, are shown in Figure 7. Figure 7(a) shows that after initially falling, the OCR value of PEO coating stabilized at 0.669 V. In contrast, the OCP shift on PEO-B_4C coating was more involved. This process consists of two phases. During the first step, OCP is reduced slowly, starting at −0.56 V to a lesser, more enduring of −0.71 V. A minimum of 1.040 V will be the optical constant of refraction, indicating that the electrolyte has penetrated and settled on both sides of the internal barrier/external porosity layer contact at the end of level II.

The electrolyte presumably diffuses through the barrier layer before coating with CS B_4C-AA7075. Moreover, the SEM pictures showed that the OCP becomes stable once the composite coating saturates with electrolytes (Figures 3(a) and 3(d)). The porosity and dense barrier layers have two separate corrosion phases in PEO-B_4C coatings. Because of the PEO coating's tight molecular structure, the corrosive solution is either on its surface or within its pores (not through the PEO coating). As a result, its susceptibility to corrode is reduced (OCP is higher) compared to PEO-B_4C coating. Protective characteristics of PEO coatings evaluated in a 3.6% NaCl solution using the potent-dynamic polarized technique, as shown in Figure 7(b). Potential for corrosion (E_{corr}) and density of current (I_{corr}) for a CS coating on an AZ64 substrate are shown in Table 1. Corrosion current density condensed below the AZ64 substrate (1.127×10^4 A/cm^2) by covering the sample. The results prove that CS and PEO coatings significantly improve the substrate's resistance to corrosion. Furthermore, PEO coating had superior corrosion current density (1.703×10^8 A/cm^2) and corrosion potential (0.47 V) than the aluminum coating. According to these results, PEO treatment dramatically enhances the CS aluminum coating's resistance to corrosion.

Comparatively, the PEO-B_4C coating's possibility for corrosion and current density of 1.127 V and 3.735×10^6 A/cm^2, respectively, align with the B_4C-AA7075 coating (0.940 V and 2.031×10^6 A/cm^2, respectively) that not treated with PEO. Accordingly, the PEO-B_4C coating offers the same level of corrosion protection as the B_4C-AA7075 layer. The corrosion resistance of a B_4C-AA7075 layer is unaffected by the PEO treatment.

4. Discussion

4.1. Coating Mechanical Properties of Plasma Electrolyte Oxidation. Nanoindentation demonstrates that PEO ceramic coatings have superior mechanical properties to cold-spray metallized coatings [34]. Metal coating on aluminum-based substrates can be transformed into ceramic Al_2O_3 layers by PEO treatment [35]. Al_2O_3 cermet significantly greater hardness and elasticity than Al and its composites. As a result, it is not surprising that PEO ceramic coatings are over CS coats in terms of hardness and flexural modulus. The PEO-B_4C coating has an elastic modulus of 23.5% points higher and is 21% points tougher than the PEO layer. It may have occurred because of the induction of B_4Cs in the matrix, which has high mechanical characteristics. As mentioned in the prior report, CS B_4C-AA7075 coating has superior mechanical qualities to the CS Al coating. Increased hardness of the B_4C-AA7075 coating is the result of reinforcing the B_4C in these coatings. In addition, the tensile properties of the B_4C-AA7075 coating enhance by the high modulus B_4C. In conclusion, the mechanical properties of a B_4C coating on Al_2O_3 ceramic improved with PEO treatment compared to those on a B_4C coating on AA7075 ceramic.

4.2. Dry Wear Behavior. Compared to a CS coating, the CS + PEO duplex coating showed more excellent resistance to wear in a series of wear tests. The PEO process increases the coating's durability by adding an oxide coating to the CS coat; this is why, the duplex coating is much more durable [36]. The B_4C-AA7075 sample treated with PEO exhibited

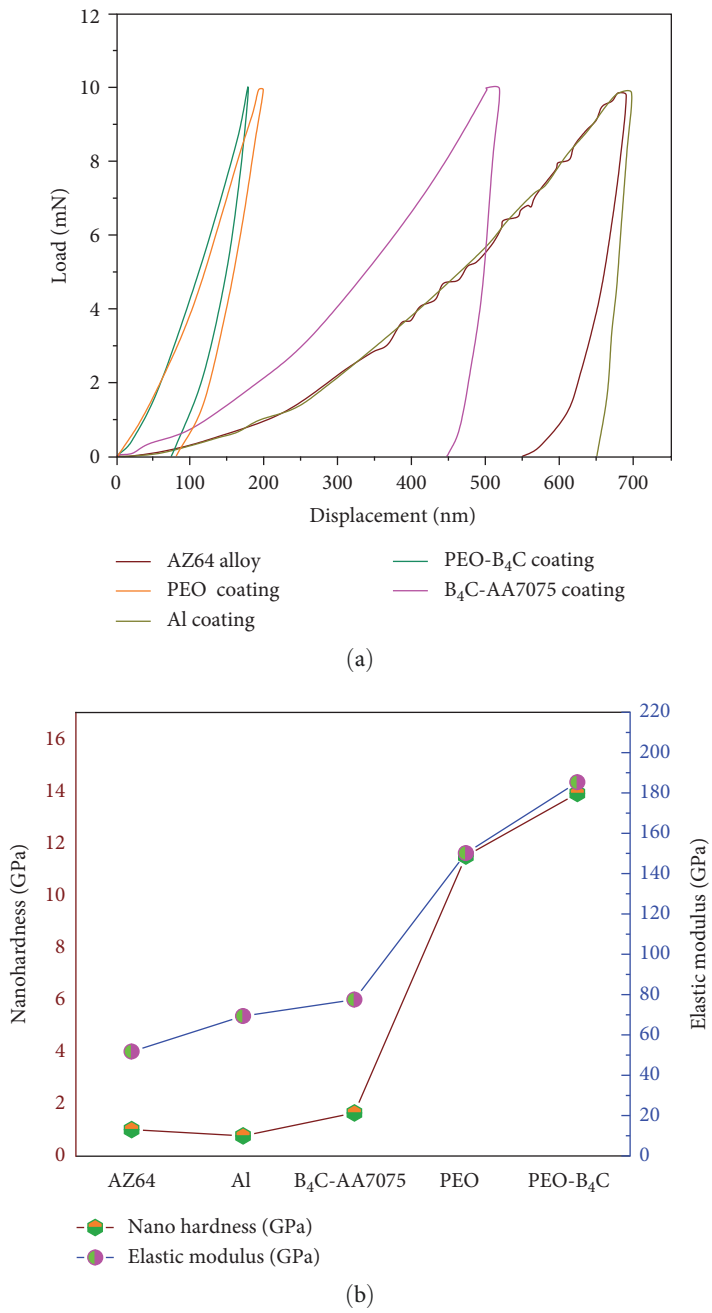

Figure 5: (a) Displacement curvature based on loads and (b) comparison of nanohardness and elastic modulus.

more excellent wear resistance than the Al sample treated with PEO. Figures 8(a) and 8(b) show a profile of the worn path in cross section for the PEO and PEO-B_4C coatings.

The PEO-B_4C coating is thinner than the PEO coating in terms of the wear track [37]. Figures 8(a) and 8(b) show a wear track formed by a PEO ceramic layer. The PEO-B_4C coating has a smaller wear track than the PEO coating. Tribological testing showed that the PEO-B_4C coating drastically reduced material removal and boosted resistance to wear [38]. In most cases, a coating made of Al_2O_3 will have a high resistance to wear because of the strong relationship between these two factors. Improved wear resistance increases the material's hardness. B_4C testing of PEO nanohardness revealed a value of 13.8 GPa, significantly higher than PEO coating (11.6 GPa). As a result, the PEO-B_4C coating offers excellent durability. The oxide layer of PEO-B_4C coating contained carbon elements (including B_4C or other types of amorphous carbon), which may serve as nanolubricants [39].

Carbon components that lubricate themselves, such as B_4C, can reduce wear volumetric loss and friction coefficient [40]. Many other elements influence and enhance the wear resistance of PEO-B_4C coatings. Due to the random

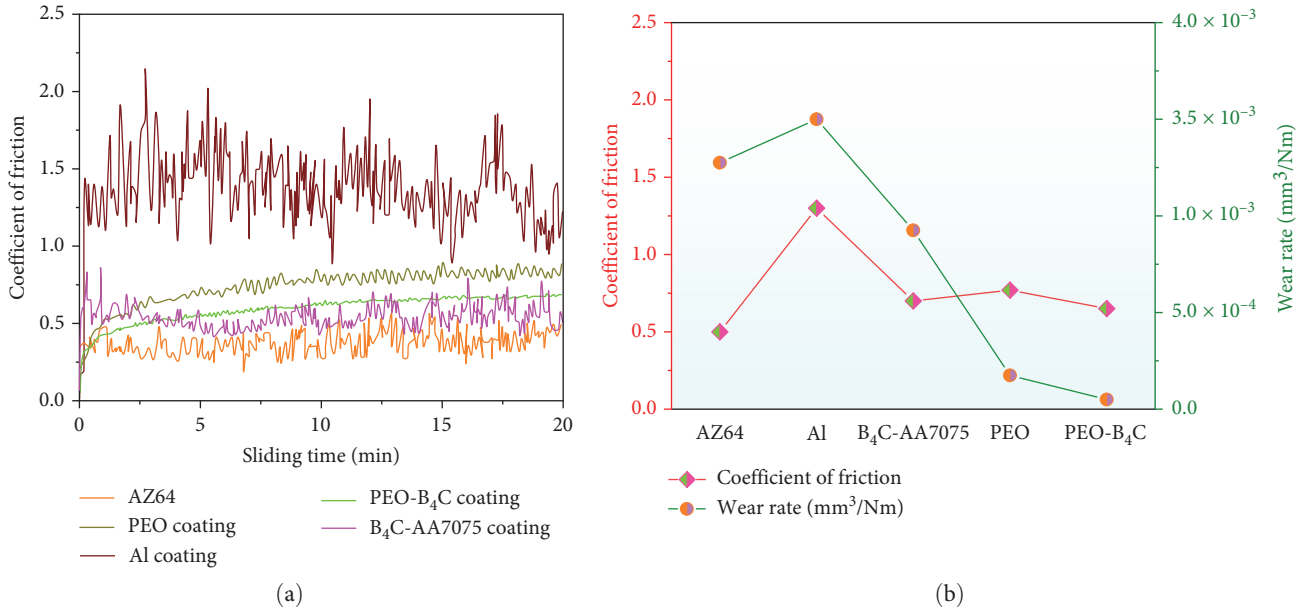

Figure 6: (a) Sliding time and friction coefficient and (b) friction coefficient and wear rate.

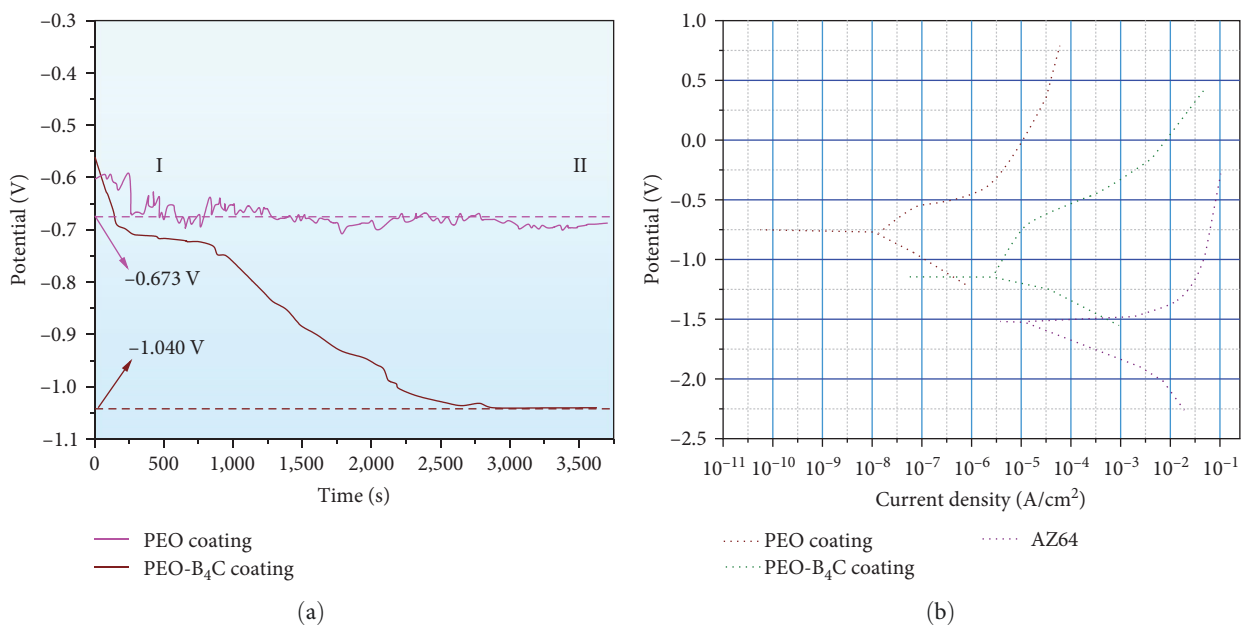

Figure 7: (a) Time responses on OCP and (b) potential vs. current density observed in 3.6 wt% NaCl solution.

distribution of microcracks in the PEO ceramic coatings, the wear tracks displayed a flaky morphology (Figures 8(c) and 8(d)). This conclusion indicates that the PEO ceramic layer wore away due to fatigue. Fatigue cracks in PEO-B_4C were more extensive than those in PEO covering. Fractures propagate in the direction of defects (pores, holes, microcracks) caused by sliding wear. However, the thick PEO-B_4C coating's porous top layer made the microcracks on the wear track more noticeable than they would have been in a PEO coating.

Table 1: Comparison of corrosion potential (E_{corr}) and current density (I_{corr}).

Examples	E_{corr} (V)	I_{corr} (A/cm^2)
Plasma electrolytic oxidation coating	−0.755	1.703×10^{-8}
Plasma electrolytic oxidation-B_4C coated	−1.127	3.735×10^{-6}
AA7075 coated	−1.225	4.660×10^{-6}
B_4C-AA7075 coated	0.940	2.031×10^{-5}
AZ64	−1.514	1.127×10^{-4}

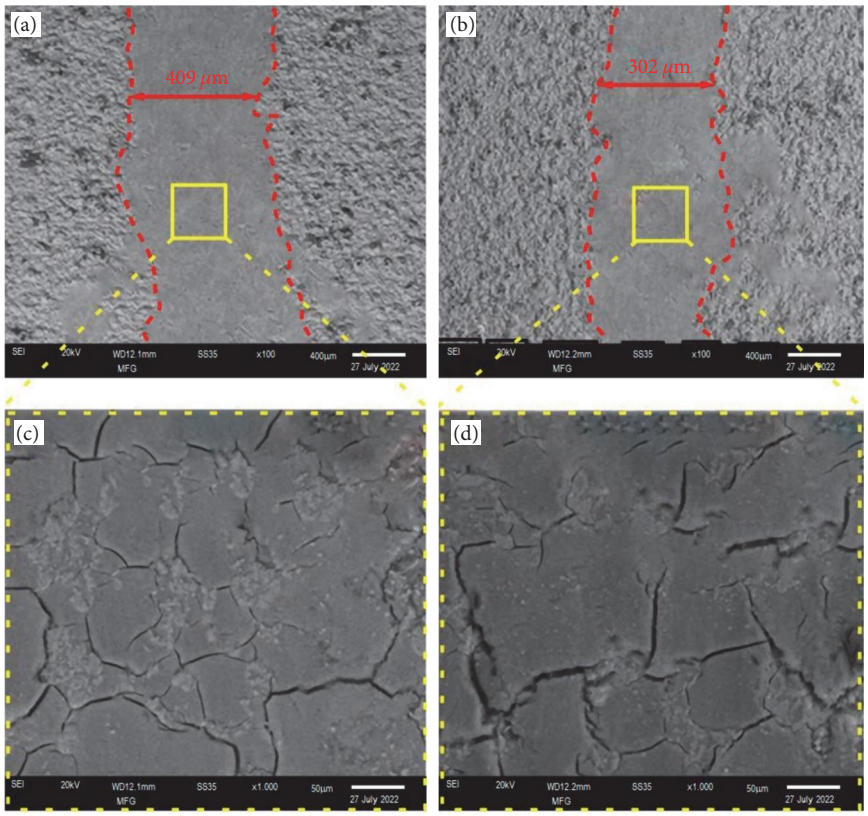

Figure 8: (a, b) SEM images and (c, d) high magnification morphology of PEO with B_4C coating.

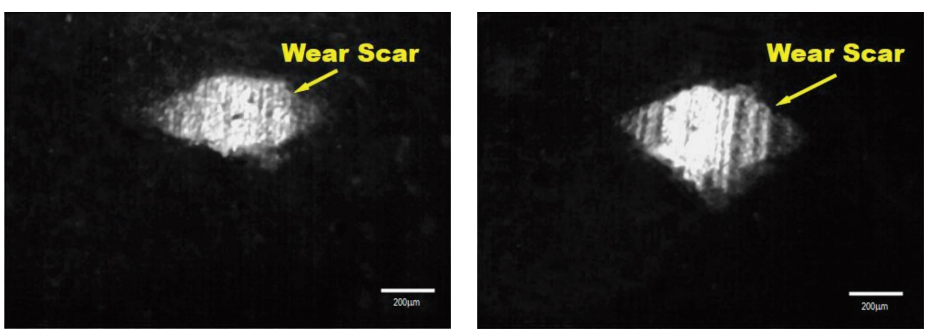

(a) (b)

Figure 9: Optical images of (a) plasma electrolyte oxidation coating and (b) plasma electrolyte oxidation + B_4C coating of the Al_2O_3 ball paired.

The PEO-B_4C coating's wear resistance is approximately a magnitude more than that of the PEO coating because of the B_4Cs self-lubricating impact [41]. Figure 9 shows an optical image showing the PEO and PEO-B_4C coatings' interaction with the Al_2O_3 spherical counterbody, where wear marks on the surface of PEO, the ceramic-coated Al_2O_3 ball. Even though the PEO ceramic coating is highly durable, the Al_2O_3 ball counterbody affects wear during the sliding process. Wear scars on the PEO-B_4C-coated Al_2O_3 ball was more noticeable than those on the PEO-coated Al_2O_3 ball. Stress wearing of the Al_2O_3 by the B_4C PEO layer's reduction in the contact area between the ball and the bearing. The COF of the PEO-B_4C coating was much smaller than that PEO layer. The homogeneous distribution of carbon components like B_4C in the PEO-B_4C coating is responsible for its better wear resistance; these elements lessen the resistance to sliding between the ceramic covering and the Al_2O_3 ball counterbodies.

4.3. Electrochemical Corrosion Analysis. The density in the aluminum coating dropped by two orders of magnitude after being treated with PEO, as shown by electrochemical corrosion testing [42]. However, the PEO treatment did not noticeably alter the B_4C-Al coating's resistance to corrosion. Coatings made of PEO were practical barriers between substrates and corrosive solutions. Its corrosion resistance

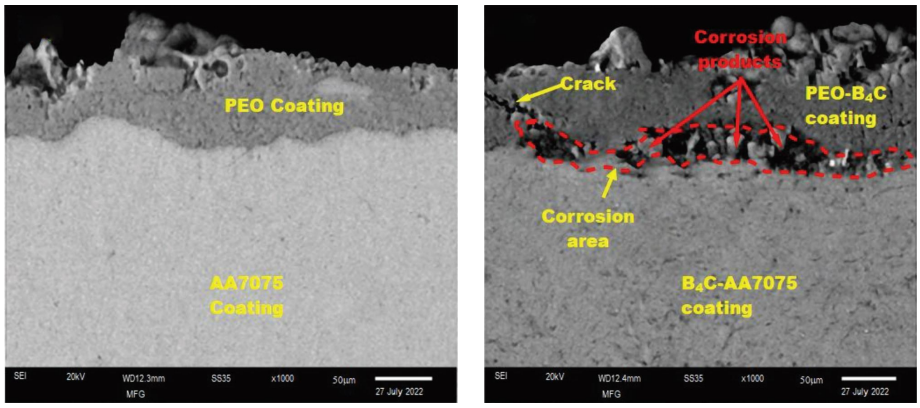

(a) (b)

Figure 10: (a) AA7075 + PEO and (b) B_4C-AA7075 + PEO cross-sectional SEM images of duplex coatings after electrochemical corrosion.

enhances by preventing corrosive media from penetrating the coating [43]. However, the substrate corroded because the electrolyte penetrated the interface through fissures and holes in PEO ceramic covering, creating channels for corrosion. Corroded specimens of aluminum+ PEO and B_4C-AA7075 + PEO twin coatings exhibit in the cross-sectional SEM image, as shown in Figures 10(a) and 10(b).

A massive corroded region is visible under the PEO-B_4C coating, as seen in Figure 10. Corrosion solution entered via fracture in PEO ceramic coating (arrow in Figure 10(b)), corroding B_4C-AA7075 coating. Instead, a cross section of PEO covering showed minimal fissures and pores [37]. As a result, the Al coating protects from corrosion. The PEO ceramic layer developed on the CS aluminum coating sample was denser and smoother than the PEO ceramic coating developed on CS B_4C-AA7075 coating specimens. It enabled more channels for the electrolyte to infiltrate through corrosion to the PEO-B_4C coating. The B_4C-AA7075 coating's corrosion resistance is not drastically altered by the PEO treatment. PEO treatment on an Al substrate creates PEO-B_4C and PEO coatings. A PEO ceramic coat applied to an Al substrate was shown to be less effective at preventing corrosion in the presence of B_4C. To further enhance its corrosion resistance, PEO-B_4C coating could benefit from the application of sealing methods.

5. Conclusion

Successful duplex coatings on AZ64 alloy using the CS technique combined with PEO, including B_4C-AA7075 + PEO and AA7075 + PEO. Mechanical characteristics, wearing, and resistance to corrosion of CS+PEO duplex coatings compared to the cold-spray metallized coatings. The results of this study indicate the following:

(1) Depending on the cold-spray coating's composition, the PEO ceramic coatings included α-Al_2O_3, γ-Al_2O_3, and a trace quantity of the B_4C. The PEO-B_4C coating also had a uniform distribution of carbon.

(2) Hardness and elastic modulus improved upon the PEO-B_4C coating compared to their CS counterparts. PEO-B_4C coatings were thicker (~25 μm) than standard PEO coatings (~18 μm). It results in more significant results for hardness (13.8 GPa) and elastic modulus (185.4 GPa) for the PEO-B_4C coating (21% and 23.5% higher).

(3) Compared to the wear rates of PEO and B_4C-AA7075 coatings, PEO-B_4C coating was significantly more durable, with a rate of only 4.84×10^5 mm^3/Nm. The Al_2O_3 layer is complex, and the B_4C acts as a natural lubricant. Not only that, it also has remarkable antifriction qualities.

(4) The PEO raises aluminum coating corrosion resistivity by lowering the current density in the coating by two magnitudes. By an outcome of these defects in the B_4C-AA7075 coating, the PEO treatment did tiny to enhance the material's resistance to corrosion.

(5) The resulting duplex coating comprises CS with the PEO technique. It has superior mechanical, wear, and corrosion characteristics equated to the independent cold-spray metallized coating. This resilient that the hybrid CS-PEO method is effective in surface engineering.

Data Availability

The data used to support the findings of this study are included within the article.

Conflicts of Interest

The authors declare that they have no conflicts of interest.

References

[1] H. Soliman, M. K. Ahmed, and R. Elbadewy, "Enhanced corrosion resistance of plasma electrolytic oxidation coatings prepared on Mg alloy ZX using nano-Al_2O_3 and NaF incorporated electrolyte," *Surface Engineering*, vol. 37, no. 2, pp. 246–252, 2021.

[2] D. Han, J. Zhang, Y. Lian, P. Ji, W. Xu, and G. Tang, "Control of ZM5 alloy ignition via PEO/aluminum phosphate

composite coating," *Surface and Coatings Technology*, vol. 436, Article ID 128309, 2022.

[3] I. A. Rastegaev and A. V. Polunin, "Regularities and features of acoustic emission under plasma electrolytic oxidation of wrought Al-Mg alloy," *Journal of Physics: Conference Series*, vol. 2144, Article ID 012020, 2021.

[4] P. Długosz, A. Garbacz-Klempka, J. Piwowońska, P. Darłak, and M. Młynarczyk, "Plasma coatings on aluminium–silicon alloy surfaces," *Archives of Foundry Engineering*, vol. 21, no. 3, pp. 96–101, 2021.

[5] J. Dou, J. Wang, H. Li, Y. Lu, H. Yu, and C. Chen, "Enhanced corrosion resistance of magnesium alloy by plasma electrolytic oxidation plus hydrothermal treatment," *Surface and Coatings Technology*, vol. 424, Article ID 127662, 2021.

[6] Y. Lv, C. Zhang, Y. Zhang, Q. Wang, X. Zhang, and Z. Dong, "Microstructure and corrosion resistance of plasma electrolytic oxidized recycled Mg alloy," *Acta Metallurgica Sinica (English Letters)*, vol. 35, pp. 961–974, 2022.

[7] S. Jin, X. Ma, R. Wu et al., "Effect of carbonate additive on the microstructure and corrosion resistance of plasma electrolytic oxidation coating on Mg-9Li-3Al alloy," *International Journal of Minerals, Metallurgy and Materials*, vol. 29, pp. 1453–1463, 2022.

[8] T. C. Senocak, T. A. Yilmaz, H. F. Budak et al., "Influence of sodium pentaborate ($B_5H_{10}NaO_{13}$) additive in plasma electrolytic oxidation process on WE43 magnesium alloys," *Materials Today Communications*, vol. 30, Article ID 103157, 2022.

[9] S. N. Grigoriev, I. O. Kondratsky, B. L. Krit et al., "Protective and thermophysical characteristics of plasma-electrolytic coatings on the ultralight magnesium alloy," *Journal of Engineering Materials and Technology*, vol. 144, no. 2, Article ID 021006, 2022.

[10] J. Wang, F. Peng, X. Wu et al., "Biocompatibility and bone regeneration of PEO/Mg-Al LDH-coated pure Mg: an *in vitro* and *in vivo* study," *Science China Materials*, vol. 64, pp. 460–473, 2021.

[11] R. R. Solís, Ö. Dinc, G. Fang, M. N. Nadagouda, and D. D. Dionysiou, "Activation of inorganic peroxides with magnetic graphene for the removal of antibiotics from wastewater," *Environmental Science: Nano*, vol. 8, no. 4, pp. 960–977, 2021.

[12] M. Ahmadi and F. Ghanbari, "Organic dye degradation through peroxymonosulfate catalyzed by reusable graphite felt/ferriferrous oxide: mechanism and identification of intermediates," *Materials Research Bulletin*, vol. 111, pp. 43–52, 2019.

[13] I. M. Patil, C. P. Jijil, M. Lokanathan, A. Swami, and B. Kakade, "Mechanical activation in reduced graphite oxide/boron nitride nanocomposite electrocatalysts for significant improvement in dioxygen reduction," *Sustainable Energy & Fuels*, vol. 2, no. 1, pp. 252–261, 2018.

[14] Y. Chen, K. Cui, M. Cui et al., "Insight into the degradation of tetracycline hydrochloride by non-radical-dominated peroxymonosulfate activation with hollow shell–core Co@NC: role of cobalt species," *Separation and Purification Technology*, vol. 289, Article ID 120662, 2022.

[15] L. Dong, Y. Li, X. Chen, D. Zhang, and Y. Guan, "ZIF-67 loaded on Fe_3O_4–MnO_2 as efficient peroxymonosulfate activator for rapid degradation of carbamazepine," *Advanced Materials Interfaces*, vol. 8, no. 11, Article ID 2100178, 2021.

[16] Y. Gerasymchuk, A. Wędzyńska, and W. Stręk, "Liquid "syngas" based on supercritical water and graphite oxide/TiO_2 composite as catalyst for CO_2 to organic conversion," *Catalysis Letters*, vol. 152, pp. 2840–2851, 2022.

[17] K. Zhang, D. Sun, C. Ma, G. Wang, X. Dong, and X. Zhang, "Activation of peroxymonosulfate by $CoFe_2O_4$ loaded on metal–organic framework for the degradation of organic dye," *Chemosphere*, vol. 241, Article ID 125021, 2020.

[18] H. Wang, Y. Xue, B. Zhu et al., "CeO_2 nanowires stretch-embedded in reduced graphite oxide nanocomposite support for Pt nanoparticles as potential electrocatalyst for methanol oxidation reaction," *International Journal of Hydrogen Energy*, vol. 42, no. 32, pp. 20549–20559, 2017.

[19] J. J. Rueda-Márquez, J. Moreno-Andrés, A. Rey et al., "Post-treatment of real municipal wastewater effluents by means of granular activated carbon (GAC) based catalytic processes: a focus on abatement of pharmaceutically active compounds," *Water Research*, vol. 192, Article ID 116833, 2021.

[20] Q. Meng, K. Wang, Y. Tang et al., "Facile synthesis of porous flower-like Co_3O_4-SiO_2 composite for catalytic decoloration of rhodamine B," *ChemistrySelect*, vol. 2, no. 32, pp. 10442–10448, 2017.

[21] X. Xu, Y. Li, G. Zhang, F. Yang, and P. He, "NiO-$NiFe_2O_4$-rGO magnetic nanomaterials for activated peroxymonosulfate degradation of rhodamine B," *Water*, vol. 11, no. 2, Article ID 384, 2019.

[22] X. Zhao, Q.-D. An, S.-F. Bo et al., "Highly efficient dynamic degradation of methylene blue on hierarchical nitrogen/cobalt-co-doped carbonaceous beads with diffusion promoting nanostructures," *ChemNanoMat*, vol. 5, no. 6, pp. 802–813, 2019.

[23] X. Qin, P. Shi, H. Liu et al., "Magnetic M_xO_y@N-C as heterogeneous catalysts for the catalytic oxidation of aniline solution with sulfate radicals," *Journal of Nanoparticle Research*, vol. 19, Article ID 225, 2017.

[24] M. Kohantorabi, G. Moussavi, S. Mohammadi, P. Oulego, and S. Giannakis, "Photocatalytic activation of peroxymonosulfate (PMS) by novel mesoporous Ag/ZnO@$NiFe_2O_4$ nanorods, inducing radical-mediated acetaminophen degradation under UVA irradiation," *Chemosphere*, vol. 277, Article ID 130271, 2021.

[25] X. Li, Q. Zou, Y. Wei et al., "Graphite assisted room-temperature synthesis of structurally defected OMS-2 nanorods for peroxymonosulfate activation," *Applied Surface Science*, vol. 497, Article ID 143770, 2019.

[26] S. Fadaei, M. Noorisepehr, H. Pourzamani et al., "Heterogeneous activation of peroxymonosulfate with Fe_3O_4 magnetic nanoparticles for degradation of Reactive Black 5: batch and column study," *Journal of Environmental Chemical Engineering*, vol. 9, no. 4, Article ID 105414, 2021.

[27] T. Zeng, S. Li, J. Hua et al., "Synergistically enhancing Fenton-like degradation of organics by *in situ* transformation from Fe_3O_4 microspheres to mesoporous Fe, N-dual doped carbon," *Science of The Total Environment*, vol. 645, pp. 550–559, 2018.

[28] G. Rotella and D. Umbrello, "Numerical simulation of surface modification in dry and cryogenic machining of AA7075 alloy," *Procedia CIRP*, vol. 13, pp. 327–332, 2014.

[29] G. Rotella, L. Settineri, D. Umbrello, O. W. Dillon Jr., and I. S. Jawahir, "Finite element modeling of microstructural changes in turning of *AA7075-T651* alloy and validation," *Proceedings of NAMRI/SME*, vol. 40, pp. 481–490, 2012.

[30] "2nd International conference on sustainable energy resources, materials and technologies, ISERMAT 2019," *Materials Science Forum*, vol. 979, Article ID 196, 2020.

[31] S. Pan, T. Saso, N. Yu et al., "New study on tribological performance of AA7075-TiB_2 nanocomposites," *Tribology International*, vol. 152, Article ID 106565, 2020.

[32] V. M. Posuvailo, V. V. Kulyk, Z. A. Duriagina, I. V. Koval'chuck, M. M. Student, and B. D. Vasyliv, "The effect of electrolyte composition on the plasma electrolyte oxidation and phase composition of oxide ceramic coatings formed on 2024 aluminium alloy," *Archives of Materials Science and Engineering*, vol. 105, no. 2, pp. 49–55, 2020.

[33] Z. Shahri, S. R. Allahkaram, R. Soltani, and H. Jafari, "Study on corrosion behavior of nano-structured coatings developed on biodegradable as cast Mg–Zn–Ca alloy by plasma electrolyte oxidation," *Surface and Coatings Technology*, vol. 347, pp. 225–234, 2018.

[34] K. Qian, W. Li, X. Lu et al., "Effect of phosphate-based sealing treatment on the corrosion performance of a PEO coated AZ91D Mg alloy," *Journal of Magnesium and Alloys*, vol. 8, no. 4, pp. 1328–1340, 2020.

[35] G. A. Mengesha, J. P. Chu, B.-S. Lou, and J.-W. Lee, "Effects of processing parameters on the corrosion performance of plasma electrolytic oxidation grown oxide on commercially pure aluminum," *Metals*, vol. 10, no. 3, Article ID 394, 2020.

[36] P. Vishwakarma, S. Soni, and P. M. Mishra, "Effect of reinforcement and volume fraction on mechanical behaviour of AA7075/B_4C/fly-ash MMCp," *International Journal of Engineering and Advanced Technology*, vol. 8, no. 4, pp. 1503–1510, 2019.

[37] J. Veerasundaram, K. Kani, R. Nallumuthu, and M. Thangaraj, "Experimental and theoretical investigation of extrusion load for AA6063/SiC extruded composite billet," *Proceedings of the Institution of Mechanical Engineers, Part E: Journal of Process Mechanical Engineering*, 2022.

[38] S. Ebrahimi, A. Bordbar-Khiabani, and B. Yarmand, "Immobilization of rGO/ZnO hybrid composites on the Zn substrate for enhanced photocatalytic activity and corrosion stability," *Journal of Alloys and Compounds*, vol. 845, Article ID 156219, 2020.

[39] E. Nikoomanzari, A. Fattah-alhosseini, M. R. P. Alamoti, and M. K. Keshavarz, "Effect of ZrO_2 nanoparticles addition to PEO coatings on Ti–6Al–4V substrate: microstructural analysis, corrosion behavior and antibacterial effect of coatings in Hank's physiological solution," *Ceramics International*, vol. 46, no. 9, pp. 13114–13124, 2020.

[40] D. S. Chandra Mouli and R. Umamaheswara Rao, "Optimization of friction stir process parameters for micro-hardness and wear characteristics of silicon carbide-reinforced Al-7075 surface composite," *Transactions of the Indian Institute of Metals*, vol. 74, pp. 3135–3143, 2021.

[41] C. P. Luo, J. Liu, and H. Liu, "Effects of Al/Zn ratio on the microstructure and strengthening of Mg-Al-Zn alloys," *Materials Science Forum*, vol. 488-489, pp. 205–210, 2005.

[42] S. Vijay Ananth, R. Srimurugan, V. Jayaseelan, A. Geethan, and J. Francis Xavier, "Experimental investigation on superplastic forming behavior of AA 6063/SiCp using stir casting," *AIP Conference Proceedings*, vol. 2283, no. 1, Article ID 020118, 2020.

[43] V. Jayaseelan, S. Vijayananth, J. Francis Xavier, S. Ajith Arul Daniel, N. M. Kumar, and X. X. Jiang, "Experimental investigation on bi-axial superplastic forming characteristics of AA6063/SiCp with various percentages of SiCp under various temperatures and pressures," *Results in Physics*, vol. 15, Article ID 102624, 2019.